INTERNATIONAL JOURNAL FOR NUMERICAL METHODS IN FLUIDS
Int. J. Numer. Meth. Fluids 2009; **61**:1029–1052
Published online 20 January 2009 in Wiley InterScience (www.interscience.wiley.com). DOI: 10.1002/fld.1995

Development of a moving artificial compressibility solver on unified coordinates

Yang-Yao Niu[1,*,†,‡], Yi-Hsun Lin[1], W. H. Hui[2] and Chien C. Chang[2]

[1]*Department of Mechanical Engineering, Chung-Hua University, Hsin-Chu 30067, Taiwan*
[2]*Division of Mechanics, Research Center for Applied Sciences, Academia Sinica, Tapei 11529, Taiwan*

SUMMARY

Based on the unified Eulerian and Lagrangian coordinate transformations, the unsteady incompressible Navier–Stokes equations with artificial compressibility effects are developed. As we know, the Eulerian coordinates cause excessive numerical diffusion across flow discontinuities, slip lines in particular. The Lagrangian coordinates, on the other hand, can resolve slip lines sharply but cause severe grid deformation, resulting in large errors and even breakdown of the computation. Recently, Hui *et al*. (*J. Comput. Phys.* 1999; **153**:596–637) have introduced a unified coordinate system that moves with velocity $h\mathbf{q}$, $\mathbf{q}$ being the velocity of the fluid particle. It includes the Eulerian system as a special case when $h=0$, and the Lagrangian when $h=1$, and was shown for the two-dimensional unsteady Euler equations of compressible flow to be superior than both Eulerian and Lagrangian systems. In the framework of unified coordinates, our work will derive the unsteady incompressible flow equations and moving geometry equations, when $h\mathbf{q}$ equals grid velocity in conservation form and is updated simultaneously during each time step. Thus, the accurate estimation of geometry conservation and controlling the grid velocity or the h value based on the unified approach can keep numerical stability and avoid computation breakdown caused by moving body or boundary layers (considered as slip lines in Lagrangian coordinates). Also, the existing high-resolution Riemann solver can be extended to discretize the current unified incompressible flow equations. Our benchmark tests including the lid-driven cavity flow and backward step flow, oscillating flat plat and pulsating stenotic tube are used to validate the computations. The results verify the accuracy and robustness of the unified artificial compressibility solver on the moving body simulation. Copyright © 2009 John Wiley & Sons, Ltd.

Received 6 May 2008; Revised 7 October 2008; Accepted 3 December 2008

KEY WORDS: unified coordinates; incompressible flow; moving body simulation; geometry conservation law; artificial compressibility fluid–structure interaction

*Correspondence to: Yang-Yao Niu, Department of Mechanical Engineering, Chung-Hua University, Hsin-Chu 30067, Taiwan.
†E-mail: yniu@chu.edu.tw
‡Professor.

Contract/grant sponsor: Visiting Scholar Summer Program of Academia Sinica
Contract/grant sponsor: National Science Foundation; contract/grant number: NSC 97-2221-E-216-009-MY2
Contract/grant sponsor: Computing Facility of National Center for the High-Performance Computing

1. INTRODUCTION

Since a long time ago, the moving body simulation has been an important topic in the computational fluid dynamics studies and widely seen in many industry applications such as aeroelasticity, fluid–structure interaction, flow-induced vibration, deformable blood artery and heart flows. To our knowledge, a reliable approach to control dynamically deforming computational domain is a key issue to achieve accurate simulation of moving body flow problems. During the past works, both Eulerian [1] and Lagrangian approaches have been widely used in this area. Based on the Eulerian coordinates, numerical convective flux is inclined to cause excessive numerical diffusion due to the fixed computational cells in space while fluid particles move across cell interfaces in any direction. Slip lines are smeared badly and shocks are also smeared, albeit better recently than slip lines. Moreover, the smearing of slip lines ever increases with time and distance unless special treatments, such as artificial numerical compression or subcell resolution, are employed [2], which are, however, not always reliable. In this regard, it is interesting to note that some works using the ghost fluid method [3] based on the empirical isobaric fix have just appeared that give good slip line and shock resolution.

Another alternative way to deal with dynamic mesh is to rely on the so-called Lagrangian method. Computational cells in the Lagrangian coordinates, on the other hand, are literally fluid particles. Consequently, it is capable of producing sharp slip line resolution due to no convective flux across cell interfaces with minimized numerical diffusion. However, the disadvantage is that the computational cells exactly follow fluid particles, always bring severe grid deformation, causing inaccuracy and even breakdown of the computation once the fluid velocity is used as the mesh moving velocity [4, 5]. To prevent this from happening, the most famous Lagrangian method in use at the present time—the arbitrary Lagrangian–Eulerian (ALE) technique—uses continuous rezoning. In order to overcome the disadvantages of Lagrangian method, in the 1970s, Hirt *et al.* [6] and Pracht [7] invented the ALE technique; see Margolin [8] for more details. However, ALE requires continuous interpolations of flow variables and computational geometry that may result in unnecessary numerical inaccuracy. Recently, to understand the connection between the Lagrangian method and the Eulerian approach, Wagner [9] first proved the equivalence of Euler and Lagrangian equations of gas dynamics for weak solutions. Also, Liou and Loh [4] and Liu [5] proposed an extended Lagrangian Method. Furthermore, a unified Eulerian and Lagrangian coordinate transformation was proposed by Hui *et al.* [10] to solve the Euler equations and achieve sharp resolution of the contact line correctly. As we know, in the framework of unified coordinates approach, the fluid equations and geometric evolution equations are written in a combined conservative form, which is different from the fluid equations alone in the pure Eulerian approach [3]. The hybrid-type coordinate system considers the flow variables to be functions of time and of some permanent identification of pseudo-particles, which move with velocity hq, q being the velocity of fluid particles. It includes the Eulerian coordinates as special case when $h=0$ and the Lagrangian when $h=1$. The unified coordinate system decides the grid velocity set to be hq, where q is the fluid velocity and h is a parameter that is determined by constraint conditions, such as the mesh alignment with the slip surface, or keeping grid angle during the mesh movement. Therefore, the grid velocity can be changed locally according to the value of h. With a prescribed grid velocity, the inviscid flow equations are written in a conservative form in the computational domain (λ, ξ, η), as well as the geometric conservation laws that control the mesh deformation. Therefore, numerical diffusion across the slip line can be reduced to a minimum with the crisp capturing of the contact discontinuity. This method was also extended to three-dimensional inviscid

DOI: 10.1002/fld

flow problems [11] and to shallow water wave problems [12]. In addition, Jin and Xu [13] recently provide another alterative to simulate the low Reynolds number flow based on gas-kinetic BGK model. Their gas-kinetic solver has been developed in a moving frame on the unified coordinates and has achieved many successful calculations of the flows with free surface and moving boundaries near the low-speed laminar flow regime. However, the applicability of gas-kinetic-type solver on the calculations of complex incompressible flows such as vortex shedding or turbulence is still unknown and needs more verification.

Regarding utilizing the unified coordinate approach to simulate the compressible viscous flow problems, a preliminary work to solve the two-dimensional Navier–Stokes equations, for solving steady viscous flows, has been performed by Hui *et al.* [14]. Their motivations are that the unified coordinate system has already been shown to work better than the Eulerian approach for inviscid flow problems. In many applications, viscous effects such as boundary layer and viscous vortex may be important. The question is: can the unified coordinate system work for computing boundary layer flows and vortex flows while keeping its advantages of resolving slip lines sharply in the inviscid flow cases? This question is important since we know that the classical Lagrangian approach fails to work for viscous flow computations due to infinite deformation of boundary cells. Shear layers can be considered as superposition of an infinite number of slip lines. The advantages of the unified coordinate system in resolving the slip lines are expected to make sense in viscous flow computations.

In this work, we would like to derive the incompressible flow equations using the unified coordinate transformation. In the framework of unified coordinates, the unsteady artificial compressibility-based incompressible flow equations are derived and the related moving geometry equations can be achieved in conservation form and updated simultaneously during each time step. Thus, the accurate estimation of geometry conservation and controlling the grid velocity based on the unified approach are expected to avoid severe grid deformation and computation breakdown caused by moving body or boundary layers (considered as slip lines in Lagrangian coordinates). Also, a unified artificial compressibility approach is developed to simulate the moving body flows with viscous effects and fluid–structure interaction. It is well known that one of the popular numerical algorithms for the calculation of incompressible flows is originated from Chorin's artificial compressibility method [15, 16]. This strategy has been applied on many steady and unsteady incompressible flow problem by Pan and Chakravarthy [17], Roger and Kwak [18] using LU decomposition scheme or an implicit line relaxation in pseudo-time and applying high-order upwind interpolation method on the spatial differencing. Meanwhile, Roe-type approximate Riemann solvers are most widely used to evaluate the interface numerical flux during their works. In this work, the same numerical strategies as [19] are chosen to solve the incompressible flow equations under the unified coordinates. Test cases including the lid-driven cavity flow and backward step flow, oscillating flat plat and pulsating stenotic tube are used to verify the computations. This paper is organized as follows. Section 2 is about the derived mathematical formulation of the artificial incompressible Navier–Stokes equations in a unified coordinate system and the related eigensystems. Section 2.1 is about the description of numerical approach; Section 3 is about the validated test cases.

2. GOVERNING EQUATION

The governing equations of the flow considered are the time-dependent incompressible Navier–Stokes equations (1) in the Cartesian coordinate. After introducing the pseudo-compressibility to

DOI: 10.1002/fld

connect pressure with continuity equation based on Chorin [15, 16], the considered equations of motion of the fluid can be compactly written in the following non-dimensional conservation form as

$$\frac{\partial Q_v}{\partial t}+\frac{\partial Q}{\partial \tau}+\frac{\partial E}{\partial x}+\frac{\partial F}{\partial y}=\frac{1}{Re}[N]\nabla^2 Q \Rightarrow \frac{\partial Q_v}{\partial t}+\frac{\partial Q}{\partial \tau}+\frac{\partial E}{\partial x}+\frac{\partial F}{\partial y}=\frac{\partial E_v}{\partial x}+\frac{\partial F_v}{\partial y} \tag{1}$$

where

$$Q_v=\begin{pmatrix}0\\u\\v\end{pmatrix},\quad Q=\begin{pmatrix}p\\u\\v\end{pmatrix},\quad E=\begin{pmatrix}\beta u\\u^2+p\\uv\end{pmatrix},\quad F=\begin{pmatrix}\beta v\\uv\\v^2+p\end{pmatrix},\quad N=\begin{pmatrix}0&0&0\\0&1&0\\0&0&1\end{pmatrix}$$

$$E_v=\begin{pmatrix}0\\\dfrac{u_x}{Re}\\\dfrac{v_x}{Re}\end{pmatrix},\quad F_v=\begin{pmatrix}0\\\dfrac{u_y}{Re}\\\dfrac{v_y}{Re}\end{pmatrix}$$

Here, p is the pressure, u and v are the x- and y-components of fluid velocity. Re is the so-called Reynolds number, β is pseudo-compressibility factor, t is the physical time and τ is the so-called pseudo-compressibility time. In addition to keeping the pseudo-compressibility time derivative term original as the inner iteration during the following unsteady flow calculations, the other terms in Equation (1) will be transformed based on a coordinate transformation in [10] from the Cartesian coordinate domain (t, x, y) to the unified coordinate domain (λ, ξ, η) as

$$\begin{aligned}\mathrm{d}t&=\mathrm{d}\lambda\\ dx&=hu\,\mathrm{d}\lambda+A\,\mathrm{d}\xi+L\,\mathrm{d}\eta\\ dy&=hv\,\mathrm{d}\lambda+B\,\mathrm{d}\xi+M\,\mathrm{d}\eta\end{aligned} \tag{2}$$

where h is an arbitrary function of coordinates (λ, ξ, η) and u, v are x- and y-component of the fluid velocity q, respectively. Let

$$\frac{\mathrm{D}_h}{\mathrm{D}t}\equiv\frac{\partial}{\partial t}+hu\frac{\partial}{\partial x}+hv\frac{\partial}{\partial y} \tag{3}$$

denotes the material following the pseudo-particle, whose velocity is hq. Then it is easy to show that

$$\frac{\mathrm{D}_h\xi}{\mathrm{D}t}=0,\quad \frac{\mathrm{D}_h\eta}{\mathrm{D}t}=0 \tag{4}$$

That is, the coordinates (ξ, η) are material functions of the pseudo-particles, and hence are their permanent identifications. Accordingly, computational cells move and deform with pseudo-particles, rather than with fluid particles as in Lagrangian coordinates. Furthermore, the geometrical

DOI: 10.1002/fld

state variables (A, B, L, M) satisfy the compatibility conditions

$$\frac{\partial A}{\partial \lambda}=\frac{\partial hu}{\partial \xi}, \quad \frac{\partial L}{\partial \lambda}=\frac{\partial hu}{\partial \eta}, \quad \frac{\partial B}{\partial \lambda}=\frac{\partial hv}{\partial \xi}, \quad \frac{\partial M}{\partial \lambda}=\frac{\partial hv}{\partial \eta}, \quad \frac{\partial A}{\partial \eta}=\frac{\partial L}{\partial \xi}, \quad \frac{\partial B}{\partial \eta}=\frac{\partial M}{\partial \xi} \tag{5}$$

Reversing the role of the independent variables, we can have

$$\begin{pmatrix} \mathrm{d}\lambda \\ \mathrm{d}\xi \\ \mathrm{d}\eta \end{pmatrix}=\frac{1}{AM-BL}\begin{pmatrix} AM-BL & 0 & 0 \\ -h(uM-vL) & M & -L \\ -h(vA-uB) & -B & A \end{pmatrix}\begin{pmatrix} \mathrm{d}t \\ \mathrm{d}x \\ \mathrm{d}y \end{pmatrix}=\frac{1}{\Delta}\begin{pmatrix} \Delta & 0 & 0 \\ -hI & M & -L \\ -hJ & -B & A \end{pmatrix}\begin{pmatrix} \mathrm{d}t \\ \mathrm{d}x \\ \mathrm{d}y \end{pmatrix} \tag{6}$$

where $\Delta=AM-BL$, $I=uM-vL$, $J=Av-uB$.

From the above transformation matrix, we can get the following chain rules for the derivatives of the dependent variables and fluxes:

$$\begin{aligned} \frac{\partial \bar{Q}_v}{a}\partial\lambda &= \frac{\partial Q_v}{\partial \lambda}\times\frac{\Delta}{\Delta} \\ \frac{\partial \bar{E}}{\partial \xi} &= \frac{\partial Q_v}{\partial \xi}\times\frac{-hI}{\Delta}+\frac{\partial E}{\partial \xi}\times\frac{M}{\Delta}+\frac{\partial F}{\partial \xi}\times\frac{-L}{\Delta} \\ \frac{\partial \bar{F}}{\partial \eta} &= \frac{\partial Q_v}{\partial \eta}\times\frac{-hJ}{\Delta}+\frac{\partial E}{\partial \eta}\times\frac{-B}{\Delta}+\frac{\partial F}{\partial \eta}\times\frac{A}{\Delta} \end{aligned} \tag{7}$$

Based on the above transformation (1), the governing equation becomes

$$\frac{\partial \bar{Q}_v}{\partial \lambda}+\frac{\partial Q}{\partial \tau}+\frac{\partial \bar{E}}{\partial \xi}+\frac{\partial \bar{F}}{\partial \eta}=\frac{\partial \bar{E}_v}{\partial \xi}+\frac{\partial \bar{F}_v}{\partial \eta} \tag{8}$$

where $\bar{Q}$ is a preserved variable vector, $\bar{E}$, $\bar{F}$ are flux vectors and $\bar{E}_v$ and $\bar{F}_v$ are viscous terms given by

$$\bar{Q}_v=\begin{pmatrix} 0 \\ u \\ v \\ A \\ B \\ L \\ M \end{pmatrix}, \quad Q=\begin{pmatrix} p \\ u \\ v \\ 0 \\ 0 \\ 0 \\ 0 \end{pmatrix}, \quad \bar{E}=\begin{pmatrix} \dfrac{\beta I}{\Delta} \\ \dfrac{1}{\Delta}(Iu(1-h)+pM) \\ \dfrac{1}{\Delta}(Iv(1-h)-pL) \\ -hu \\ -hv \\ 0 \\ 0 \end{pmatrix}, \quad \bar{F}=\begin{pmatrix} \dfrac{\beta J}{\Delta} \\ \dfrac{1}{\Delta}(Ju(1-h)-pB) \\ \dfrac{1}{\Delta}(Jv(1-h)+pA) \\ 0 \\ 0 \\ -hu \\ -hv \end{pmatrix}$$

DOI: 10.1002/fld

$$\bar{E}_v = \begin{pmatrix} 0 \\ u_\xi \dfrac{1}{Re}\left(\dfrac{M^2+L^2}{\Delta^2}\right) - u_\eta \dfrac{1}{Re}\left(\dfrac{BM+LA}{\Delta^2}\right) \\ v_\xi \dfrac{1}{Re}\left(\dfrac{M^2+L^2}{\Delta^2}\right) - v_\eta \dfrac{1}{Re}\left(\dfrac{BM+LA}{\Delta^2}\right) \\ 0 \\ 0 \\ 0 \\ 0 \\ 0 \end{pmatrix} \tag{9}$$

$$\bar{F}_v = \begin{pmatrix} 0 \\ v_\eta \dfrac{1}{Re}\left(\dfrac{A^2+B^2}{\Delta^2}\right) - v_\xi \dfrac{1}{Re}\left(\dfrac{BM+LA}{\Delta^2}\right) \\ v_\eta \dfrac{1}{Re}\left(\dfrac{A^2+B^2}{\Delta^2}\right) - v_\xi \dfrac{1}{Re}\left(\dfrac{BM+LA}{\Delta^2}\right) \\ 0 \\ 0 \\ 0 \\ 0 \\ 0 \end{pmatrix}$$

As required in constructing the Riemann solutions of the inviscid flux of the system equation (8), we need to consider the hyperbolicity property of Equation (8) to ensure the existence and uniqueness of the solution to the Riemann problem; now we check this: the eigensystem of (8) can be found by direct computation of the Jacobian matrix. The Jacobian matrix of the transformation from Cartesian coordinates to unified coordinates is defined as we assume $k_x = M/\Delta$, $k_y = -L/\Delta$, $\theta = I/\Delta$

$$A = \frac{\partial \bar{E}}{\partial Q} = \begin{bmatrix} 0 & \beta k_x & \beta k_y \\ k_x & (k_x u+\theta)(1-h) & k_y u(1-h) \\ k_y & k_x v(1-h) & (k_y v+\theta)(1-h) \end{bmatrix} \tag{10}$$

A similar transformation for the Jacobian matrix is introduced as

$$A = X \Lambda X^{-1} \tag{11}$$

and its three distinct eigenvalues $\Lambda = \mathrm{diag}[\lambda_1, \lambda_2, \lambda_3]$ as

$$\Lambda = \begin{bmatrix} \theta(1-h) & 0 & 0 \\ 0 & \theta(1-h)+C & 0 \\ 0 & 0 & \theta(1-h)-C \end{bmatrix} \tag{12}$$

where $C = \sqrt{\theta^2(1-h)^2 + \beta(k_x^2+k_y^2)}$.

DOI: 10.1002/fld

Based on the eigenvalue of (12), the corresponding right eigenvectors can be obtained as

$$X=\begin{bmatrix} 0 & -C(\theta h-C) & C(\theta h+C) \\ k_y & uh-k_x(\theta h-C) & uh-k_x(\theta h+C) \\ -k_x & vh-k_y(\theta h-C) & vh-k_y(\theta h+C) \end{bmatrix} \tag{13}$$

and

$$X^{-1}=\frac{1}{C^2}\begin{bmatrix} (vk_x-uk_y)h & v\theta h^2+\beta k_y & -(u\theta h^2+\beta k_x) \\ \frac{1}{2} & \frac{1}{2}k_x(\theta h+C) & \frac{1}{2}k_y(\theta h+C) \\ \frac{1}{2} & \frac{1}{2}k_x(\theta h-C) & \frac{1}{2}k_y(\theta h-C) \end{bmatrix} \tag{14}$$

From the above derived eigenvalues and the right eigenvector, it is shown that the eigenvectors are linearly independent, forming a completed basis in the state space. The system equations (8) are therefore regarded as hyperbolic for all values of h as shown in the eigenvalues (12). This includes the Eulerian coordinates as a special case when $h=0$ and the Lagrangian one when $h=1$. As we have known from Hui's works [10, 11], it is shown that the smooth solutions of the system of two-dimensional Euler equations of gas dynamics written in the classical Lagrangian coordinates are equivalent to the same system written in the unified coordinates with $h=1$. The steps of the proof can easily be repeated for the current artificial compressibility flow equations to show that its weak hyperbolicity existed on the classical Lagrangian coordinates. To avoid possible numerical difficulties arising from the lack of a completed set of eigenvectors, we shall use $0\leqq h<1$ to keep the hyperbolic character of the artificial compressibility equations.

2.1. Moving body strategy

As noted in [14], pathlines are identical with streamlines in steady flow. Hence, a slip line coincides with the streamline of a fluid particle and, therefore, also with the streamline of a pseudo-particle. Consequently, it can be taken to correspond to one of the coordinates, η say, thus avoiding the Godunov averaging across it. Hence, in the unified coordinate system a slip line can be sharply resolved. This is in direct contrast to the Eulerian coordinates, where a slip line does not coincide with a coordinate line and, as a result, the Godunov averaging across a slip line in a computational cell will forever smear it. For unsteady flow, pathlines are in general distinct from streamlines. While a slip line still coincides with the pathline of a fluid particle, it does not always coincide with a streamline. Hence, a slip line does not always coincide with a coordinate line in the unified coordinate system. In using the unified coordinate system for flow computation, once the grid is set initially it is subsequently generated by the motion of the pseudo-particles. The unique feature of transformation (2) is that it depends on the flow through $\mathbf{Q}=h\mathbf{q}$, i.e. $U=hu$, $V=hv$. In the general case, h is arbitrary. In this regard, numerical experiments [1] clearly indicate the trend that slip line resolution increases with increasing h from $h=0$ (Eulerian) to $h=1$ (Lagrangian) and the unified coordinates using grid-angle preserving $0\leqq h\leqq 1$ yield better slip line resolution than the Eulerian coordinates. Furthermore, h may be chosen as an advantage to avoid excessive numerical diffusion in the Eulerian coordinates, and/or to avoid severe grid deformation in the Lagrangian coordinates.

In practice, we separate the eight equations of (8) into two groups: the physical conservation laws (the first three equations) and the geometric conservation laws (the last four equations in

DOI: 10.1002/fld

(8) in every numerical time step. First, we solve the first three equations based on the Riemann-type solver for the physical conservation laws while keeping (A, B, L, M) fixed. This yields the updated values of $(\Delta p, \Delta u, \Delta v)$ until achieving convergence in every physical time step, which, after decoding, gives the updated values of (A, B, L, M) to match with the geometric conservation laws. Here, we propose the grid velocity as

$$hu = x_t, \quad hv = y_t \tag{15}$$

for the moving body simulation. Then substituting Equations (15) into the coordinate transformation (2), we can easily achieve a widely used coordinate transformation as

$$\begin{aligned} \mathrm{d}t &= \mathrm{d}\lambda \\ \mathrm{d}x &= x_\lambda \mathrm{d}\lambda + x_\xi \mathrm{d}\xi + x_\eta \mathrm{d}\eta \\ \mathrm{d}y &= y_\lambda \mathrm{d}\lambda + y_\xi \mathrm{d}\xi + y_\eta \mathrm{d}\eta \end{aligned} \tag{16}$$

So the geometrical state variables (A, B, L, M) in Equation (12) become $(x_\xi, y_\xi, x_\eta, y_\eta)$ like those in Equation (16). Thus, the geometrical state variables $(x_\xi, y_\xi, x_\eta, y_\eta)$ at the cell interface in each time evolution can be updated based on the compatibility conditions as

$$\begin{aligned} \frac{\partial A}{\partial \lambda} &= \frac{\partial x_\lambda}{\partial \xi} \\ \frac{\partial B}{\partial \lambda} &= \frac{\partial y_\lambda}{\partial \xi} \\ \frac{\partial L}{\partial \lambda} &= \frac{\partial x_\lambda}{\partial \eta} \\ \frac{\partial M}{\partial \lambda} &= \frac{\partial y_\lambda}{\partial \eta} \end{aligned} \tag{17}$$

Similarly, conditions (17) can also update the cell area as $\Delta = AM - BL$, which is the so-called Jacobian transformation from the Cartesian coordinates to unified coordinates. The procedures from Equation (15) to Equation (17) automatically coincide with the geometry conservation law, which is required in the moving body flow calculations.

3. NUMERICAL IMPLEMENTATION

3.1. Grid velocity

To keep the geometry conservation law, the derived equation (17) at each cell interface can be numerically discretized as

$$\begin{aligned} A^{n+1} &= A^n + \frac{\Delta\lambda}{\Delta\xi}[(x_\lambda)_{i+1/2} - (x_\lambda)_{i-1/2}] \\ B^{n+1} &= B^n + \frac{\Delta\lambda}{\Delta\xi}[(y_\lambda)_{i+1/2} - (y_\lambda)_{i-1/2}] \end{aligned} \tag{18}$$

DOI: 10.1002/fld

$$L^{n+1} = L^n + \frac{\Delta\lambda}{\Delta\eta}[(x_\lambda)_{j+1/2} - (x_\lambda)_{j-1/2}]$$
$$M^{n+1} = M^n + \frac{\Delta\lambda}{\Delta\eta}[(y_\lambda)_{j+1/2} - (y_\lambda)_{j-1/2}]$$

where n denotes the physical time step and the grid velocity at each cell interface can be calculated by a second-order backward difference as

$$\frac{\partial x^n}{\partial\lambda} = \frac{3x^n - 4x^{n-1} + x^{n-2}}{2\Delta\lambda}$$

and

$$\frac{\partial y^n}{\partial\lambda} = \frac{3y^n - 4y^{n-1} + y^{n-2}}{2\Delta\lambda} \tag{19}$$

3.2. Time integration of physical equations

To implement the time evolution of the first three governing equations, usually the physical time term is discretized using a second-order, three-point, backward difference formula; that is

$$\frac{\partial\tilde{Q}_v}{\partial\lambda} = \frac{1.5\tilde{Q}_v^{n+1,p+1} - 2\tilde{Q}_v^n + 0.5\tilde{Q}_v^{n-1}}{\Delta\lambda} \tag{20}$$

where n designates the index of the physical time level and p is the index of the artificial time level. The artificial time term is discretized by the following implicit Euler finite-difference formula:

$$\frac{\partial Q}{\partial\tau} = \frac{Q^{n+1,p+1} - Q^{n+1,p}}{\Delta\tau} \tag{21}$$

Based on Equations (20) and (21), the linearized governing Equation (1) can be written as

$$\left(\frac{1.5}{J\Delta t} + \frac{1}{J\Delta\tau} + \frac{\partial A}{\partial\xi} + \frac{\partial B}{\partial\eta} - \frac{\partial A_v}{\partial\xi} - \frac{\partial B_v}{\partial\eta}\right)\Delta Q^p$$
$$= -\frac{1.5\tilde{Q}_v^p - 2\tilde{Q}_v^n + 0.5\tilde{Q}_v^{n-1}}{\Delta t} - \left(\frac{\partial(\tilde{E} - E_v)}{\partial\xi} + \frac{\partial(\tilde{F} - F_v)}{\partial\eta}\right)^p$$
$$= -\mathrm{Res}(Q)^p \tag{22}$$

The above equation can be factorized using the LU decomposition method for the pseudo-time iteration. $\mathrm{Res}(Q)$ is the unsteady residue vector, ΔQ is the spatial difference $Q_{i+1} - Q_i$. $\Delta\tau$ is chosen as the local pseudo-time step that is determined by the largest eigenvalue of the preconditioning system of governing equations for each grid cell. The diffusion terms are evaluated by the standard central differencing scheme. The implicit part at the left-hand side of Equation (22) is discretized using a first-order upwind difference scheme. One of them in the ξ-direction can be expressed as

$$\frac{\partial A}{\partial\xi} = \frac{(A_{i+1,j,k} - A_{i,j,k})}{\Delta\xi} \tag{23}$$

DOI: 10.1002/fld

where $A=A^{+}+A^{-}$. $A^{+}$and A^{-} are computed based on the eigenvalues of the matrix A and the related eigenvector T and its inverse T^{-1} as shown in the following equation:

$$A^{\pm}=T\Lambda^{\pm}T^{-1} \tag{24}$$

$$\Lambda=\begin{pmatrix}\lambda_1 & 0 & 0 & 0 & 0\\ 0 & \lambda_2 & 0 & 0 & 0\\ 0 & 0 & \lambda_3 & 0 & 0\\ 0 & 0 & 0 & \lambda_4 & 0\\ 0 & 0 & 0 & 0 & \lambda_5\end{pmatrix} \tag{25}$$

Similarly B and C are calculated. Equation (22) can be factored after using finite-difference formulation for the derivative term as

$$[(D-L)D^{-1}(D+U)]\Delta Q_{i,j}^{n+1,k+1}=J\Delta\tau\,\mathrm{Res}(Q)^{n+1,k} \tag{26}$$

where L, D and U are recursively as

$$L=\frac{\Delta\tau}{\Delta\xi}\left[-A^{+}_{i-1,j,k}+\frac{1}{2}(A_v)_{i-1,j,k}\right]+\frac{\Delta\tau}{\Delta\eta}\left[-B^{+}_{i,j-1,k}+\frac{1}{2}(B_v)_{i,j-1,k}\right] \tag{27}$$

and

$$D=I+\frac{3\Delta\tau}{2\Delta t}+\frac{\Delta\tau}{\Delta\xi}\left[A^{-}_{i,j,k}\frac{1}{2}(A_v)_{i,j,k}\right]+\frac{\Delta\tau}{\Delta\eta}\left[B_{i,j,k}-\frac{1}{2}(B_v)_{i,j,k}\right] \tag{28}$$

and

$$U=\frac{\Delta\tau}{\Delta\xi}\left[A^{+}_{i+1,j,k}-\frac{1}{2}(A_v)_{i+1,j,k}\right]+\frac{\Delta\tau}{\Delta\eta}\left[B^{+}_{i,j+1,k}-\frac{1}{2}(B_v)_{i,j+1,k}\right] \tag{29}$$

Furthermore, numerical calculations of Equation (26) can be proceeded using the LU approach, as advance solution in pseudo-time is implemented in two steps: a backward and forward step in each direction given as

$$\text{First}\quad (D-L)\Delta Q^{*}=\mathrm{RHS}^{n+1,k+1/2} \tag{30}$$

Then

$$(D+U)\Delta Q^{n+1,k+1}=D\Delta Q^{*} \tag{31}$$

Finally, the primitive variables at the new pseudo-time level $k+1$ is then updated by

$$Q^{n+1,k+1}=Q^{n+1,k}+\Delta\tilde{Q}^{*} \tag{32}$$

3.3. Flux extrapolation

To achieve the high-order accurate flux approximation, one of the possibilities can be relied on the third-order accurate upwinding flux extrapolation for the derivatives ∂E_ξ that have the form. A third-order upwind flux at the cell interface $i+\frac{1}{2}$ is defined by

$$\tilde{E}_{i+1/2}=\tfrac{1}{2}[\tilde{E}(Q_{j+1})+\tilde{E}(Q_j)]+\tfrac{1}{6}[\Delta\tilde{E}^{+}_{i-1/2}-\Delta\tilde{E}^{+}_{i+1/2}+\Delta\tilde{E}^{-}_{i+1/2}-\Delta\tilde{E}^{-}_{i+1/2}] \tag{33}$$

DOI: 10.1002/fld

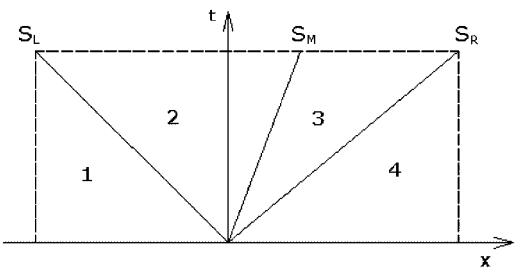

Figure 1. A structure of wave patterns of one-dimensional Riemann problem.

Where $\Delta f^{\pm}$ is the flux across positive or negative traveling waves. The flux difference is taken as

$$\Delta \tilde{E}^{\pm}_{i+1/2} = A^{\pm}(\bar{Q})\Delta Q_{i+1/2} \tag{34}$$

where A represents the Jacobian matrix. The A^+ and A^- matrices are computed first by forming a diagonal matrix of the positive eigenvalues and multiplying through by the similarity transform, and since the A^+ matrix plus the A^- matrix equal the original Jacobian matrix, we have

$$\begin{aligned} A^+ &= X\Lambda X^{-1} \\ A^- &= A - A^+ \end{aligned} \tag{35}$$

where X is the matrix of right eigenvectors of A, X^{-1} is its inverse. The flux difference is evaluated at the midpoint by using the average of Q

$$\bar{Q} = \tfrac{1}{2}(Q_{j+1} + Q_{j+1}) \tag{36}$$

The primary problem with using schemes of accuracy greater than second order occurs at the boundaries. Large stencils will require special treatment at the boundaries, and a reduction of order is necessary; therefore, when going to a higher-order accurate scheme, compactness is desirable.

As noted in [20] and shown in Figure 1, the structure of the analytical solution of one-dimensional Riemann problem contains three wave families separating four constant states from left to right states as $Q_{\mathrm{L}}, Q^*_{\mathrm{L}}, Q^*_{\mathrm{R}}, Q_{\mathrm{R}}$. These states $Q^*_{\mathrm{L}}, Q^*_{\mathrm{R}}$ emerge from the interaction of the data states $Q^*_{\mathrm{L}}, Q^*_{\mathrm{R}}$ and compose the so-called the star region. The left and right waves are either shock or rarefaction denoted as the two acoustic waves $S_{\mathrm{L}}$and S_{R} seen in Figure 1; all flow quantities change across these waves, the change being discontinuous across shocks. The middle wave is always a shear wave S_{M} across $Q^*_{\mathrm{L}}, Q^*_{\mathrm{R}}$. The solution strategy is based on the fact that both Q^*_{L} and Q^*_{R} are constant throughout the star region.

Harten *et al.* [20] proposed various simplifications to the internal structure of the Riemann fan by taking integral averages of the conserved variables over sections of the fan. The most elaborate solver suggested by Harten *et al.* [20] is a two-state HLL approximation in which two-state averages are computed, one from the left-most acoustic wave to the contact wave and one from the contact to the right-most acoustic wave, the detail of this scheme is rather cumbersome. Harten, Lax and van Leer also proposed an approximated Riemann solver to find a inviscid flux vector E^* in the star region, However, Toro *et al.*'s HLLC [21] showed that a significant simplification could be made by assuming the particle velocity to be constant across the Riemann fan. Moreover, Batten *et al.* [22] have shown that with a suitable choice of all wave speeds. Toro *et al.*'s two-state HLLC

DOI: 10.1002/fld

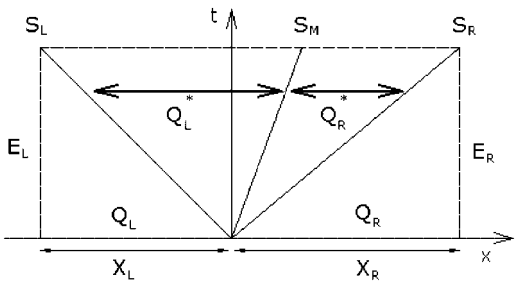

Figure 2. A two-intermediate wave pattern of one-dimensional Riemann problem.

solver resolves isolated shock and contact/shear waves exactly and is positively conservative in the definition of Einfeldt *et al.*'s [23] split of the star fluxes E_{L}^{*} and E_{R}^{*} based on states Q_{L}^{*}, Q_{R}^{*}. This version of the HLLC-type fluxes will be defined as follows:

$$\overline{E}=\begin{bmatrix}\beta\theta\\ \theta u(1-h)+Pk_x\\ \theta v(1-h)+Pk_y\end{bmatrix} \tag{37}$$

The HLLC flux considers two averaged intermediate states, Q_{L}^{*}, Q_{R}^{*} separated by the contact wave, whose speed is denoted by S_{M} as seen in Figure 2. The two-state approximate Riemann solution was defined by Harten *et al.* [20] as

$$Q_{\mathrm{HLLC}}=\begin{cases}Q_{\mathrm{L}} & \text{if } S_{\mathrm{L}}>0\\ Q_{\mathrm{L}}^{*} & \text{if } S_{\mathrm{L}}\leqslant 0\leqslant S_{\mathrm{M}}\\ Q_{\mathrm{R}}^{*} & \text{if } S_{\mathrm{M}}\leqslant 0\leqslant S_{\mathrm{R}}\\ Q_{\mathrm{R}} & \text{if } S_{\mathrm{R}}<0\end{cases} \tag{38}$$

The corresponding interface flux, denoted as F_{HLLC}, is

$$E_{\mathrm{HLLC}}=\begin{cases}E_{\mathrm{L}} & \text{if } S_{\mathrm{L}}>0\\ E_{\mathrm{L}}^{*}(Q_{\mathrm{L}}^{*}) & \text{if } S_{\mathrm{L}}\leqslant 0\leqslant S_{\mathrm{M}}\\ E_{\mathrm{R}}^{*}(Q_{\mathrm{R}}^{*}) & \text{if } S_{\mathrm{M}}\leqslant 0\leqslant S_{\mathrm{R}}\\ E_{\mathrm{R}} & \text{if } S_{\mathrm{R}}<0\end{cases} \tag{39}$$

Harten *et al*. suggested various ways of the exact solutions Q^{*} between two acoustic waves. The HLLC flux is a modification of HLL. Instead of a single intermediate state Q^{*}, two intermediate states, Q_{L}^{*} and Q_{R}^{*}, are assumed, separated by an interface moving with the speed S_{M}. To calculate Q_{L}^{*} and Q_{R}^{*}, we recap the approach taken by Batten *et al.* by applying the Rankine–Hugoniot conditions across the shear wave. However, the simplest approach for computing these star states was suggested by Toro *et al.*, who ignored the influence of expansion fans and made the particle

DOI: 10.1002/fld

velocity constant between the acoustic waves. Applying the Rankine–Hugoniat condition across the S_L and S_R waves gives

$$\begin{aligned} E_L^* &= E_L + S_L(Q_L^* - Q_L) \\ E_R^* &= E_R + S_R(Q_R^* - Q_R) \end{aligned} \tag{40}$$

where S_L, S_R are taken from Einfeldt *et al.* [23] as $S_L = \theta_L(1-h) - C_L$ and $S_R = \theta_R(1-h) - C_R$. Based on Equation (9), the rearrangement of the left-side flux of star region, we can obtain $S_L Q_L^* - \overline{E}_L^* = S_L - Q_L - \overline{E}$, namely

$$S_L \begin{bmatrix} P_L^* \\ u_L^* \\ v_L^* \end{bmatrix} - \begin{bmatrix} \beta\theta_L^* \\ u_L^*\theta_L^*(1-h) + P_L^* k_x \\ v_L^*\theta_L^*(1-h) + P_L^* k_y \end{bmatrix} = S_L \begin{bmatrix} P_L \\ u_L \\ v_L \end{bmatrix} - \begin{bmatrix} \beta\theta_L \\ u_L\theta_L(1-h) + P_L k_x \\ v_L\theta_L(1-h) + P_L k_y \end{bmatrix} \tag{41}$$

Furthermore, the speed S_M of the shear wave can be considered as a constant U^*, which is the average directed velocity between the two acoustic waves

$$S_M = \theta_L^* = \theta_R^* \tag{42}$$

Then the system equation (41) can be rewritten and separated as

$$P_L^* = P_L + \frac{\beta(S_M - \theta_L)}{S_L} \tag{43}$$

$$u_L^* = \frac{u_L(S_L - \theta_L(1-h))}{S_L - \theta_L^*(1-h)} + \frac{\beta(S_M - \theta_L)k_x}{(S_L - \theta_L^*(1-h))S_L} \tag{44}$$

$$v_L^* = \frac{v_L(S_L - \theta_L(1-h))}{S_L - \theta_L^*(1-h)} + \frac{\beta(S_M - \theta_L)k_y}{(S_L - \theta_L^*(1-h))S_L} \tag{45}$$

Then the conserved variables at the left-hand side of the star region are rearranged as

$$\theta_L^* = \begin{bmatrix} P_L + \dfrac{\beta(S_M - \theta_L)}{S_L} \\ S^* \\ \dfrac{v_L(S_L - \theta(1-h))}{S_L - \theta_L^*(1-h)} \end{bmatrix} \tag{46}$$

with

$$S^* = \frac{S_R S_L(P_R - P_L)}{\beta(S_R - S_L)} + \frac{S_R u_L - S_L u_R}{S_R - S_L} \tag{47}$$

The same procedure can be worked for the construction of Q_R^*.

3.4. Wall model

In this work, we consider the elastic stenotic tube in the numerical tests. The fluid–structure interaction is required to be considered in the simulation. Here, wall compliance is modeled using

DOI: 10.1002/fld

an independent ring model to compute the vessel deformations [24]. This model assumes that the structural nodes move only in the radial direction. In spite of its intrinsic limitations, the extreme simplicity of this model makes it very popular. A linear elastic model equation to describe the wall motion can be written as a damped oscillator

$$m\frac{\partial^2 r}{\partial t^2}+d\frac{\partial r}{\partial t}+kr=P_{\mathrm{w}} \tag{48}$$

where $m=\rho_{\mathrm{w}}h$, $k=Eh/(1-v^2)a^2$, $d=2\sqrt{mk}$, h is the wall thickness, ρ_{w} the wall density, E Young's modulus, v the Poisson ratio, a the vessel radius, p the pressure, r the wall displacement and p_{w} the pressure force at the wall. The radial displacement of each structural node can be obtained by solving Equation (48) by using a fourth-order Runge–Kutta scheme. The fluid–structure equations (8) and (48) are solved in an uncoupled way. Both the solutions of fluid and structure equations are updated in an unsteady time marching manner. The pressure loads at the vessel wall predicted by the fluid solver are transferred to the source terms in the structure equation at the same time step. After that the wall displacement is updated at each grid point along the whole tube and vessel. Also, the wall mesh velocity can be estimated based on the last two wall displacements during the previous two time steps to achieve the second-order accurate estimation. Then, the new wall position and mesh velocity are substituted into the fluid solver and the related boundary conditions. Therefore, the updated pressure load can be re-predicted and a cycle of simulation fluid–structure interaction during the same time step is completed until the fluid–structure interaction is repeated until mass conservation criterion is satisfied in the fluid solver. However, the strategy of wall motion estimation may result in the moving grid distortion to produce excessive numerical errors. To avoid numerical instability, the geometry conservation performed by Equation (23) and a grid re-generation may be the necessary procedure.

4. NUMERICAL RESULTS

In the following test cases, we choose $h=0$, 0.5, 0.9, 1 for all the steady-state cases to keep the weak hyperbolicity for the model equations we use. In addition, we will also check the influence of h value on the convergence rate in the following cases. In the unsteady cases, Equation (15) is chosen for the moving body simulation to keep the geometry conservation law. Thus, the h value is given as grid velocity and floating with each grid node. Also, β is kept as 10 in all the cases. The test cases are:

4.1. Lid-driven cavity

The lid-driven cavity flow problem is a widely used benchmark test for the incompressible Navier–Stokes code validation. With the simplicity of geometry, the driven cavity flow contains complicated flow physics driven by multiple counter rotating vortices on the corners of the cavity depending on the Reynolds number. A very detailed discussion on computational as well as experimental studies on the lid-driven cavity flow can be found in Shankar and Deshpande [25]. As noted in their studies, different numerical method solutions found in the literature agree with each other at low Reynolds numbers ($Re=1000$). However, the solutions at higher Reynolds numbers ($Re>7500$) have noticeable discrepancies. Nevertheless, there are still very different results concerning the first Hopf bifurcation and the behavior of the solution for intermediate and high Reynolds numbers

DOI: 10.1002/fld

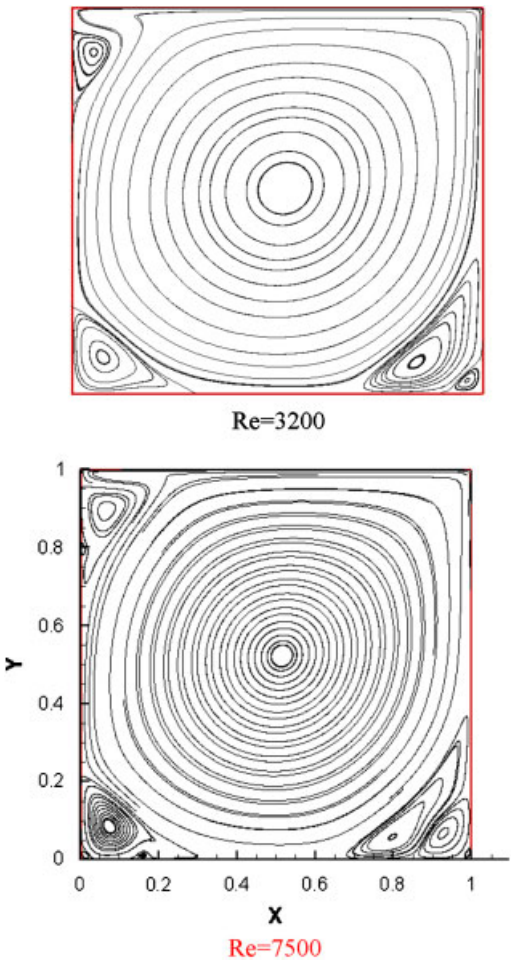

Figure 3. Streamline patterns for lid-driven cavity flow.

as seen in most of the former works [25]. It was suggested that the first Hopf bifurcation occurs around Reynolds number $Re=7500$. To avoid the unnecessary controversy validated data, the driven cavity flow with Reynolds numbers 3200 and 7500 as seen in the works of Ghia *et al.* [26] are chosen to verify numerical accuracy.

From all our comparisons we can conclude that above $Re=3200$, higher-order approximations together with the use of fine grids are necessary for accuracy. The grid independence study is necessary. The computations are performed on a 118×118 and 236×236 grid systems, which are clustered near the wall and stretched from the wall to the cavity center. Both computed results on the two grid meshes are close. Here, the results on the coarse meshes are demonstrated. The streamtrace patterns in the driven cavity flow are plotted in Figure 3. It is shown that one primary vortex near the center and three corner eddies are captured. Also one small secondary zone in the lower right corner is visible. Figures 3 exhibits the formation of the counter-rotating secondary

DOI: 10.1002/fld

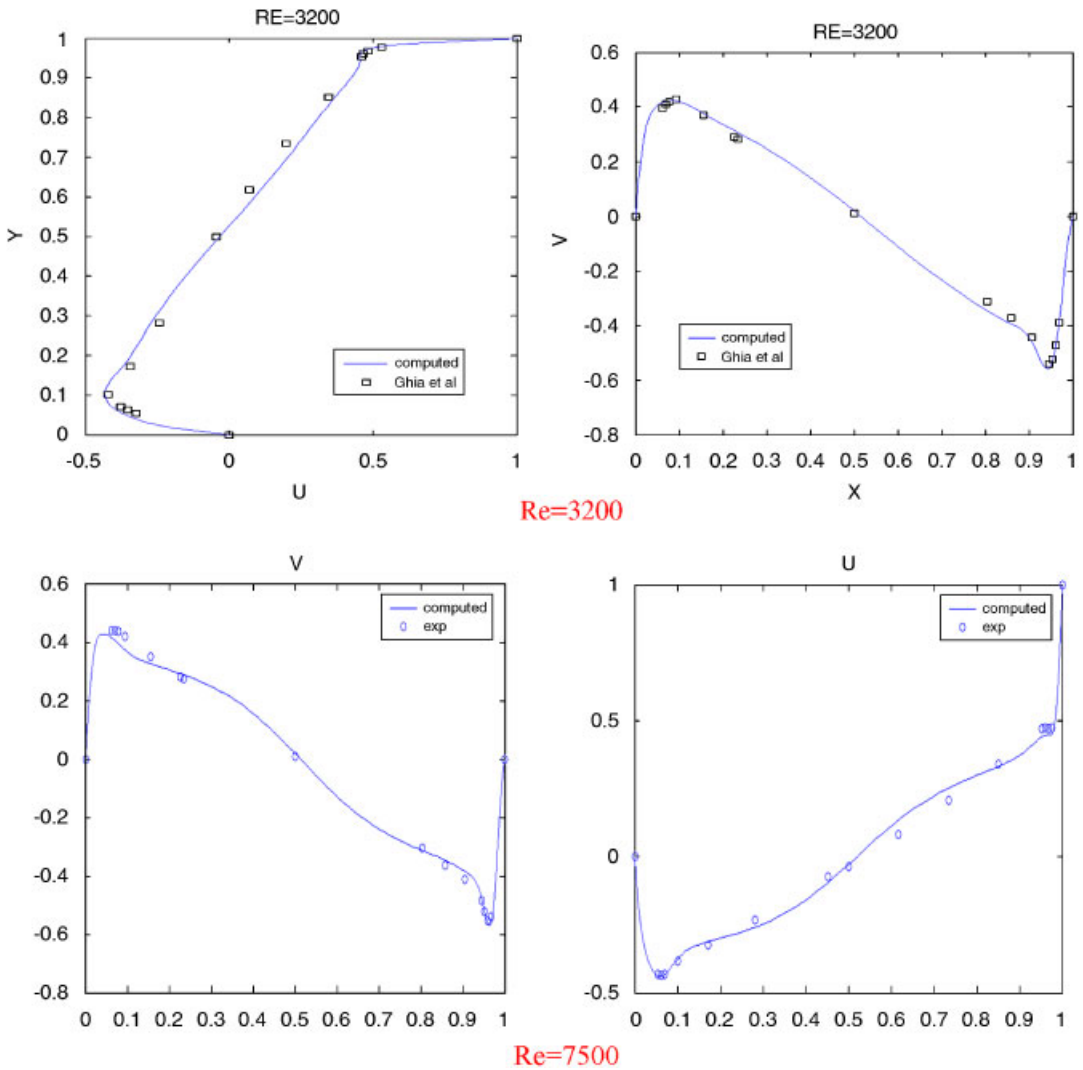

Figure 4. U velocity component along vertical centerline (left); V velocity component along horizontal centerline (right) for the driven cavity flow.

vortices that appear as the Reynolds number increases. It is evident that as the Reynolds number increases, the center of the primary vortex moves toward the geometric center of the cavity. In Figure 4, the computed u along vertical lines and v velocity along horizontal lines through the center are shown to agree with the validated data. Figure 5 shows the comparison of convergence rate against different h values. It is seen that better convergence rate is received as the h value is closer to zero in the current cavity calculations. In addition, only the computed residues of the unified approach with $h=0$ can drop to machine zero due to its pure hyperbolicity. The cases with finite h values are not achieving exact convergence.

DOI: 10.1002/fld

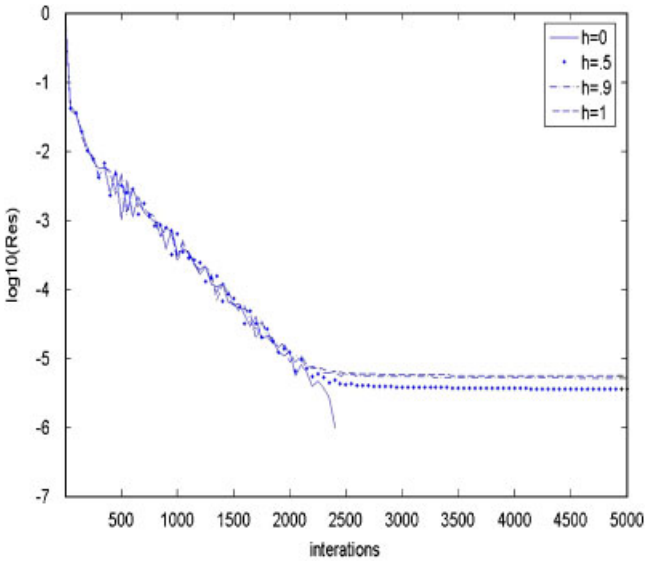

Figure 5. Comparison of convergence history for the driven cavity flow at $Re=3200$ with different h.

4.2. *Flow over a backward-facing step*

We study two-dimensional computations of laminar flow over a backward-facing step. The flow over a backward-facing step in a channel provides an excellent test case for the accuracy of numerical method because of the dependence of the reattachment length on the Reynolds number. Excessive numerical dissipations in favor of stability will result in failure to predict the correct reattachment length. The flow was assumed to be laminar, incompressible and Newtonian, and the walls were rigid with no slip conditions. The boundary of the flow domain consists of two sections with different types of boundary conditions. At the inlet boundary, a constant uniform velocity profile normal to the inlet of the inlet is used. The pressures at the inlet can be obtained from the solution of the governing equation (9) by assuming the constant velocity inside. At the outflow boundary, the condition describing the surface traction force can be assumed

$$\left(-p\delta_{ij}+\mu\left(\frac{\partial u_i}{\partial x_j}+\frac{\partial u_j}{\partial x_i}\right)\right)n_j=0 \tag{49}$$

where n_j, $j=1,2$, denote the components of the outward pointing normal unit vector at the outflow boundary. In rigid wall calculations, traction-free outflow is assumed. All the results presented are obtained using 120×51 grid points and the downstream boundary was located at $x=30h$, where h is the step height. In Figures 6 and 7, we computed the velocity distribution and the stream patterns for backward step flow to about $Re=600$ and $Re=800$. In Figure 8, numerical results for different Reynolds numbers are shown in comparison with the experimental and computational results of Orlandi [27]. The dependence of the reattachment length on Reynolds number is in good agreement with the experimental data up to about $Re=600$ and $Re=800$. In the case with $Re=800$, Figure 9 shows the comparison of convergence rate against different h values. The convergence history demonstrates that the current backward step flow simulation contained the same tendency

DOI: 10.1002/fld

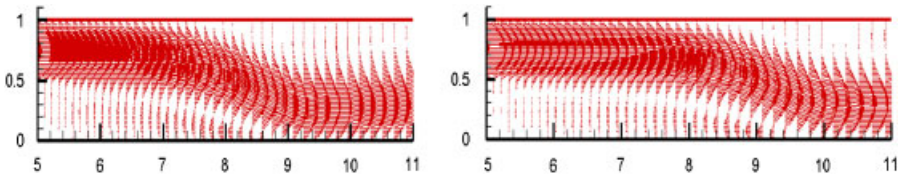

Figure 6. Velocity distribution for backward step flow $Re=600$ and $Re=800$.

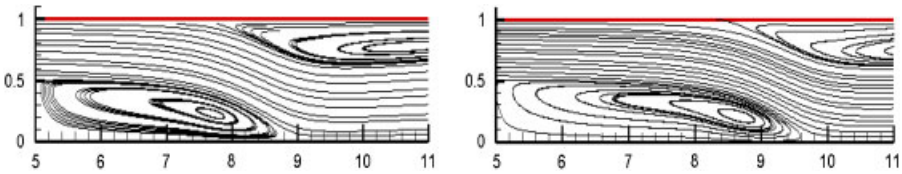

Figure 7. Stream patterns for backward step flow $Re=600$ and $Re=800$.

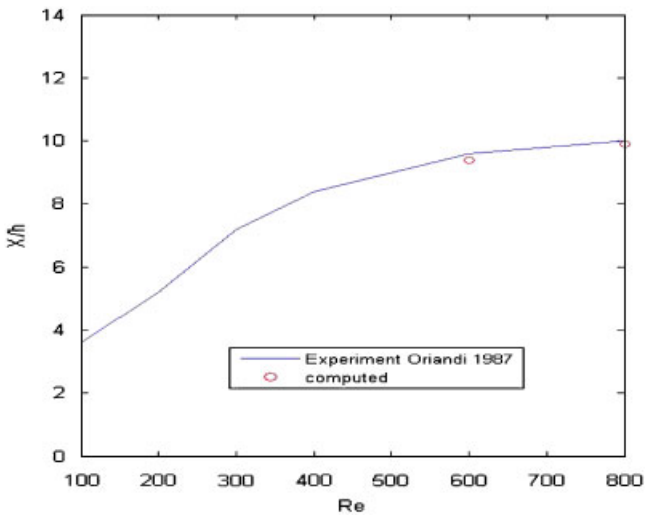

Figure 8. Comparisons of main recirculation zone length for backward step flow.

of comparison of h values against convergence rate. It is also noted that better convergence rate is received as the h value is closer to zero. In addition, only the computed residues of the unified approach with $h=0$ and $h=0.5$ can drop to machine zero due to their strong hyperbolicity.

4.3. Stokes's second problem

The Stokes's second problem seen in [28] considers fluid motion above an infinite flat plate that executes sinusoidal oscillations parallel to itself. Owing to its moving characteristics, the grid velocity equation (15) is used. Therefore, the h value is floating with grid velocity at each grid

DOI: 10.1002/fld

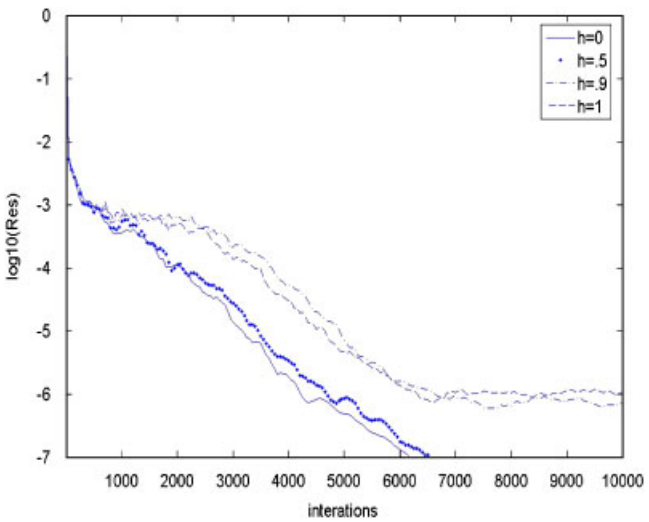

Figure 9. Comparison of convergence history for the backward step flow at $Re = 800$ with different h.

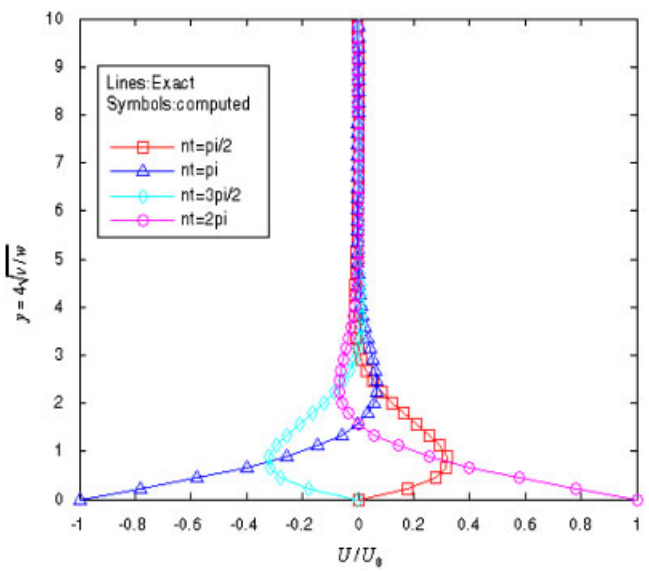

Figure 10. Velocity distributions for oscillating wall at time $wt = \pi/2$, π, $3\pi/2$ and 2π.

node during every physical time step. To start this problem, the flow over above the plate is initially assumed to be stationary. The governing equation of velocity U in the x-direction is

$$\frac{\partial U}{\partial t} = \nu \frac{\partial^2 U}{\partial y^2} \tag{50}$$

DOI: 10.1002/fld

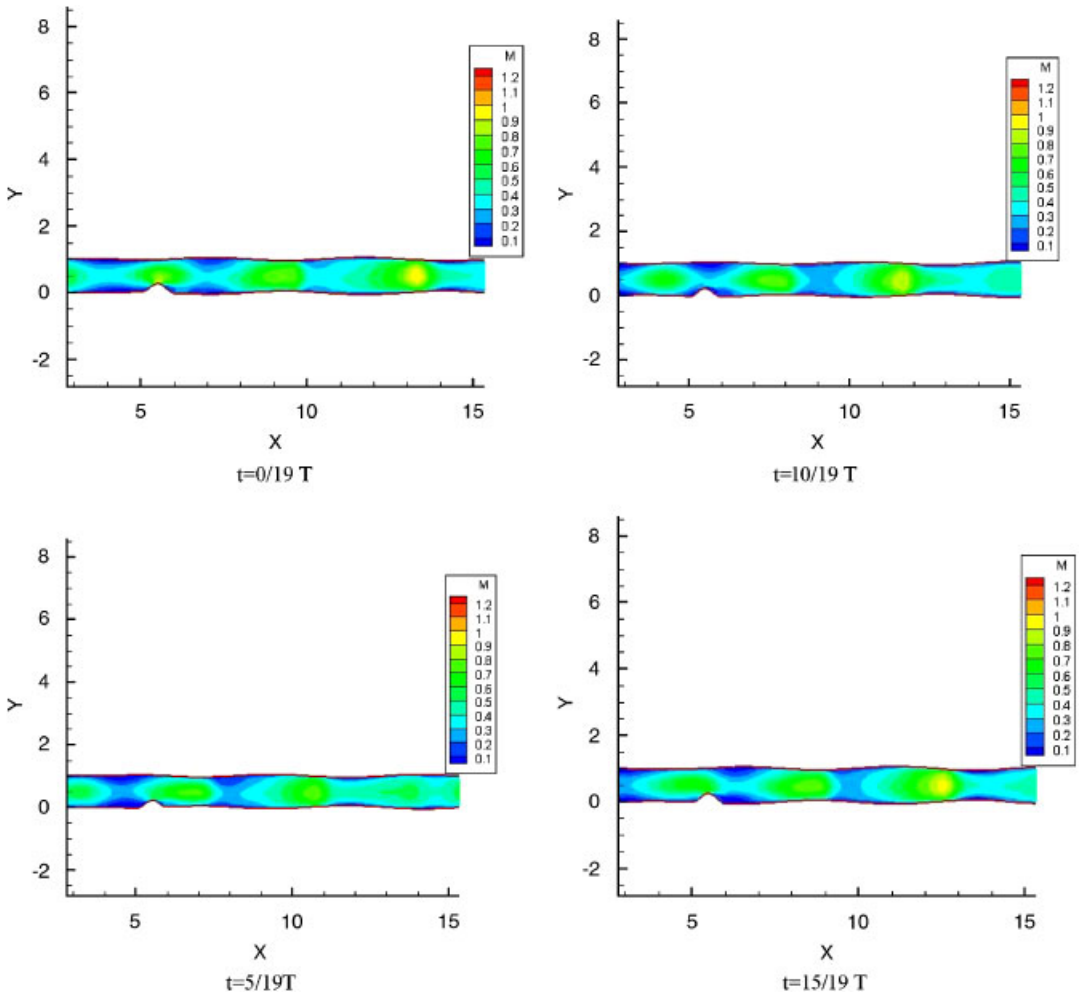

Figure 11. Velocity contour plots in a pulsatile cycle for a deformable tube.

With the boundary conditions

$$U_{\text{wall}}(0,t) = U_0 \cos wt, \quad U(\infty,t) = 0$$

The exact solution for the above problem is

$$U(y,t) = U_0 \mathrm{e}^{-y\sqrt{w/2v}} \cos(wt - y\sqrt{w/2v})$$

At $y = 4\sqrt{v/w}$, the amplitude of U is equal to $U_0 \exp(4/\sqrt{2}) = 0.05U_0$, which means that the influence from the wall is confined within a distance of order $\delta \sim 4\sqrt{v/w}$. The kinematic viscosity coefficient takes a value $v = 0.00046395$, and a mesh size of 1×50 grid points is used.

DOI: 10.1002/fld

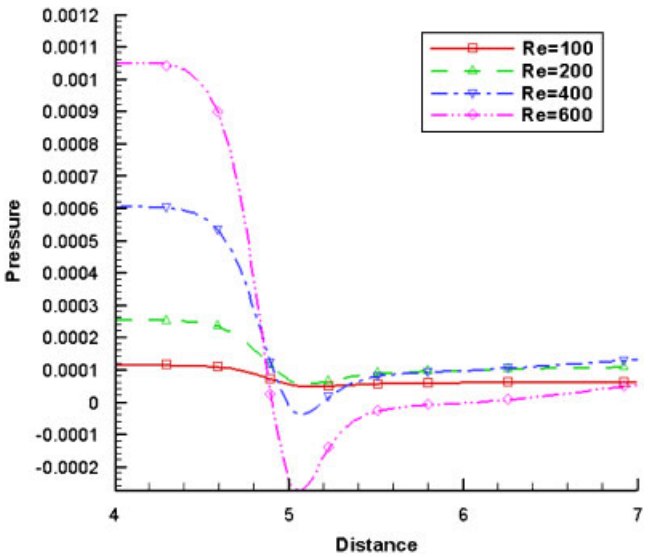

Figure 12. Variations of pressure at wall for Reynolds numbers 100, 200, 400, 600 from $X=4$ to $X=7$ at time $=\frac{3}{4}$T.

In the predicted results as shown in Figure 10, velocity distributions for oscillating wall at time $wt=\frac{\pi}{2}$, π, $\frac{3}{2}\pi$ and 2π are shown to be consistent with the exact solutions. This demonstrates the robustness and accuracy of the unified approach for the viscous computation.

4.4. Elastic stenotic tube

Subsequently, the flowfields in an elastic tube are simulated. The computation is performed based on a 200×51 grid cells. The non-dimensional geometrical parameters are as follows: inlet diameter 1, pre-stenosis length 5, and stenosis length 1; a long post-stenosis domain 31 is chosen in order to minimize the influence of downstream boundary conditions. In order to avoid considering the turbulence effects, a mild stenosis with only 25% area reduction is considered. The flow was assumed to be laminar, incompressible and Newtonian, and the walls only deform in the radial direction with the grid velocity obtained from Equation (15). Therefore, the h value is floating with grid velocity at each grid point during every physical time step. At the inlet boundary, a sinusodial incoming velocity profile as described in Equation (51) is used. The fluid–structure interaction is included in the calculations. The pressures at the inlet can be obtained from the solution of the governing equations (8), (9) by assuming a prescribed incoming velocity distribution. At the outflow boundary, as traction-free conditions Equation (49) is assumed.

$$u(\lambda)=\tfrac{1}{2}(1-\cos(2\pi\lambda)) \tag{51}$$

In this case, a Reynolds number defined at the inlet of 800 is selected. As total velocity contour plots are shown in Figure 11, it is shown that the reverse flow distal to the stenosis and the re-circulation region moves to downstream from the early systolic cycle to late diastolic cycle. Also we can find that the formation of the recirculation region is strongly effected by the compliant vessel. The separation mainly appears around the flow over the neck of the stenosis, and then

DOI: 10.1002/fld

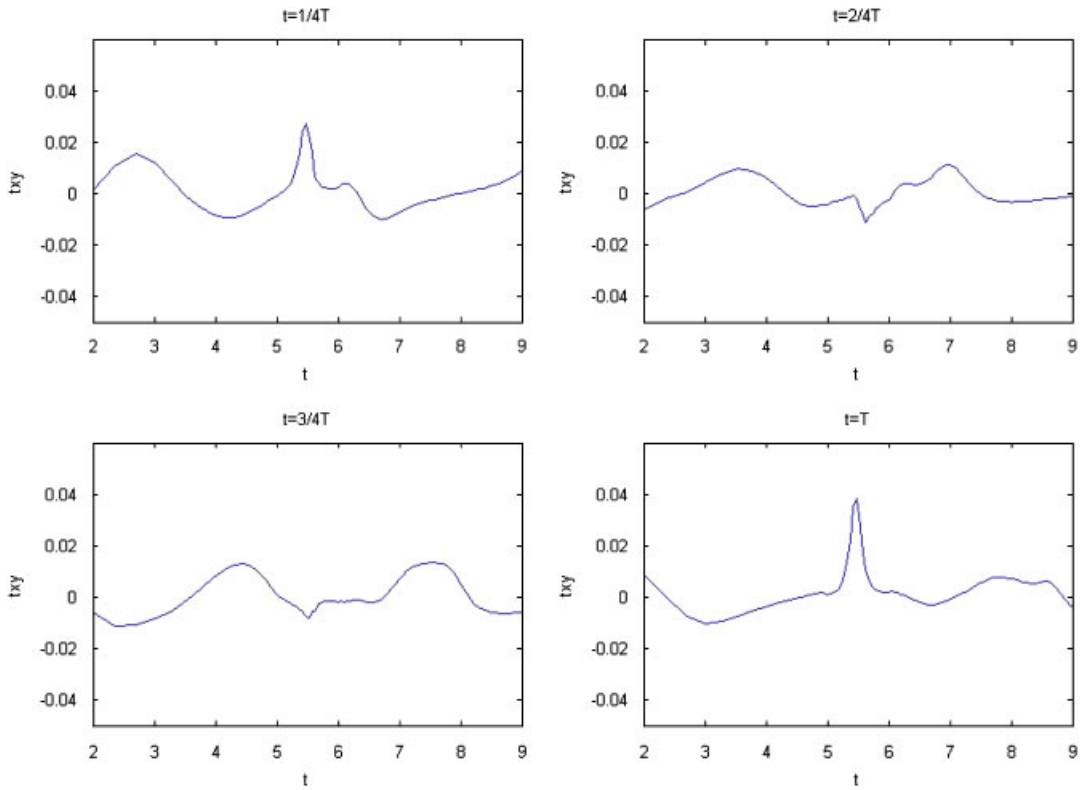

Figure 13. Variations of shear stress at stenotic wall for Reynolds number = 800 from $X = 2$ to $X = 9$ in pulsatile cycle.

it disappears around the region along the convergent wall and restarts at the beginning of the divergent wall. It is shown that the separation zone shows up periodically along the compliant vessel wall. In Figure 12, pressure distributions are shown to distribute along the stenotic wall. It is shown that the pressure drop occurs around the neck of the stenotic region in the late diastolic cycle and at the beginning of systolic cycle. Next, the pressure distributions along the stenotic region for four different Reynolds number with 100, 200, 400 and 600 are also shown in Figure 12. It is shown that the pressure drop occurs around the neck of the stenotic region, no matter what the value of Reynolds number is. A negative pressure difference is increased with the increasing Reynolds number. Furthermore, the estimations of wall shear stress distributions for the whole wall and the stenotic area are depicted in Figure 12. It is very encouraging to find that the prediction of the location of maximum wall shear stress is consistent with the analytic studies in [29], which demonstrate that the location of maximum wall shear stress is always upstream of the neck of the stenosis and independent of Reynolds number in the whole pusatile cycle. In addition, a strong oscillating wall shear stress distribution is shown to appear around the neck of the constriction-enlargement region for the lower wall, which is depicted in Figure 13. It is noted that the prediction of the location of maximum wall shear stress is always found around the beginning of enlargement and is independent of the Reynolds number. Also a positive peak of the shear stress distribution

DOI: 10.1002/fld

is found to appear on the lower aortic arch during the systole and the early diastole, and then changed as a negative peak during the late diastole.

5. CONCLUDED REMARKS

- In this paper, an unsteady artificial compressibility solver for moving body simulation based on unified coordinate approach is proposed and developed. In the framework of unified coordinates, a unified moving body approach, including the unsteady incompressible flow equations and moving geometry equations, with grid velocity as $h\mathbf{q}$ achieves conservation form and gets updated simultaneously during each time step. Accurate estimation of geometry conservation and controlling the grid velocity based on the unified approach can avoid severe grid deformation and computation breakdown caused by moving body or boundary layers (considered as slip lines in Lagrangian coordinates). In addition, the HLLC Riemann solver is developed in this study to solve artificial compressibility-type incompressible flow equations. Also, a linear elastic modeling of wall motion is included here for the consideration of the fluid–structure interaction.

ACKNOWLEDGEMENTS

The first author wishes to acknowledge the work partially supported by the Visiting Scholar Summer Program of Academia Sinica and the National Science Foundation under NSC 97-2221-E-216-009-MY2. Also, the computing facility of National Center for the High-Performance Computing, Taiwan, ROC.

REFERENCES

1. Lipinkov K, Shashkov M. The error minimization based strategy for moving mesh methods. *Communications in Computational Physics* 2006; **1**:53–80.
2. Toro EF. *Riemann Solvers and Numerical Methods for Fluid Dynamics*. Springer: Berlin, Heidelberg, 1997.
3. Fedkiw R, Aslam T, Xu S. The ghost fluid method for deflagration and detonation discontinuities. *Journal of Computational Physics* 1999; **154**:393–427.
4. Loh CY, Liou MS. A new Lagrangian method for three-dimensional steady supersonic flows. *Journal of Computational Physics* 1994; **113**:224–248.
5. Liou MS. An extended Lagrangian method. *Journal of Computational Physics* 1995; **118**:294–309.
6. Hirt CW, Amsden AA, Cook JL. An arbitrary Lagrangian–Eulerian computing method for all flow speeds. *Journal of Computational Physics* 1974; **14**:227–253.
7. Pracht W. Calculating three-dimensional fluid flows at all speeds with an Eulerian–Lagrangian computing mesh. *Journal of Computational Physics* 1975; **17**:132–159.
8. Margolin LG. Introduction to 'an abritrary Lagrangian–Eulerian computing method for all flow speeds'. *Journal of Computational Physics* 1997; **135**:198–202.
9. Wagner DH. Equivalence of Euler and Lagrangian equations of gas dynamics for weak solutions. *Journal of Differential Equations* 1987; **68**:118–136.
10. Hui WH, Li PY, Li ZW. A unified coordinate system for solving the two-dimensional Euler equations. *Journal of Computational Physics* 1999; **153**:596–637.
11. Hui WH, Koudriakov S. A unified coordinate system for solving the three-dimensional Euler equations. *Journal of Computational Physics* 2001; **172**:235–260.
12. Hui WH, Koudriakov S. Calculation of the shallow water wave equations using the unified coordinates. *SIAM Journal on Scientific Computing* 2002; **23**:1615–1654.

DOI: 10.1002/fld

13. Jin C, Xu K. A unified moving grid gas-kinetic method in Eulerian space for viscous flow computation. *Journal of Computational Physics* 2007; **222**:155–175.
14. Hui WH, Wu ZN, Gao B. Preliminary extension of the unified coordinate system approach to computation of viscous flows. *Journal of Scientific Computing* 2007; **30**(2):301–344.
15. Hoffmann KA, Chiang ST. *Computational Fluid Dynamics*, *Volume 2* (3rd edn). Engineering Education System: Wichita, Kansas, 21–46.
16. Chorin J. A numerical method for solving viscous flows problems. *Journal of Computational Physics* 1967; **2**:12–16.
17. Pan D, Chakravarthy SR. Unified formulation for incompressible flows. *AIAA Paper 89-0122*, January 1989.
18. Roger SE, Kwak D. Upwind differencing scheme for the time-accurate incompressible Navier–Stokes equations. *AIAA Journal* 1990; **28**(2):253–262.
19. Niu Y-Y, Chang C-H, Tseng W-YI, Pen H-H, Yu H-Y. Numerical simulation of an aortic flow based on a HLLC type incompressible flow solver. *Communications in Computational Physics* 2009; **5**:142–162.
20. Harten A, Lax PD, van Leer B. On upstream differencing and Godunov-type schemes for hyperbolic conservation law. *SIAM Review* 1983; **25**(1):35–61.
21. Toro EF, Spruce M, Spears W. Restoration of the contact surface in the HLL Riemann solver. *Shock Wave* 1994; **4**:25–34.
22. Batten P, Leschziner MA, Goldberg UC. Average-state Jacobians and implicit methods for compressible viscous and turbulent flows. *Journal of Computational Physics* 1997; **137**:38–78.
23. Einfeldt B, Munz CD, Roe PL, Sjogreen B. On Godunov-type methods near low densities. *Journal of Computational Physics* 1991; **92**:273–296.
24. Quarteroni A, Tuveri M, Veneziani A. Computational vascular fluid dynamics: problems, models and methods. *Computing and Visualization in Science* 1998; **2**:163–197.
25. Shankar PN, Deshpande MD. Fluid mechanics in driven cavity. *Annual Review of Fluid Mechanics* 2000; **32**:93–136.
26. Ghia PU, Ghia KN, Shih C. High-*Re* solution for incompressible flow using Navier–Stokes equations and a multigrid method. *Journal of Computational Physics* 1982; **48**:387–411.
27. Orlandi P. Vorticity–velocity formulation for high *Re* flows. *Computers and Fluids* 1987; **15**(2):137–149.
28. Currie IG. *Fundamental Mechanics of Fluids*. McGraw-Hill: New York, 1974.
29. Lee KW, Xu XY. Modelling of flow and wall behaviour in a mildly stenosed tube. *Medical Engineering and Physics* 2002; **24**:575–586.

DOI: 10.1002/fld